Uncovering low frequency band gaps in electrically resonant metamaterials through tuned dissipation and negative impedance conversion

IOP Publishing Smart Materials and Structures
Smart Mater. Struct. **31** (2022) 015002 (19pp) https://doi.org/10.1088/1361-665X/ac3434

Uncovering low frequency band gaps in electrically resonant metamaterials through tuned dissipation and negative impedance conversion

J Callanan[1], C L Willey[2,3], V W Chen[2,3], J Liu[2,3,4], M Nouh[1] and A T Juhl[2,*]

[1] University at Buffalo (SUNY), Buffalo, NY 14260, United States of America
[2] Air Force Research Laboratory, Wright-Patterson AFB, OH 45433, United States of America
[3] UES, Inc., Dayton, OH 45432, United States of America
[4] Miami University, Oxford, OH 45056, United States of America

E-mail: abigail.juhl.1@afresearchlab.com

Received 20 July 2021, revised 10 October 2021
Accepted for publication 27 October 2021
Published 16 November 2021

Abstract

A new class of electromechanically coupled metamaterial is presented which relies on magnetic field interactions between the host structure and a local resonator circuit to realize novel vibration control capabilities. The metamaterial chain exhibits a highly tunable vibration band gap which can be easily placed at a desired frequency using the resonant circuit parameters, providing a robust mechanism to independently alter the band gap width, depth, and frequency of maximum attenuation. In its dissipative form, the electromechanical metamaterial is shown to exhibit electrical metadamping as a function of the local resonance circuit resistance. The impact of the damping ratio as a function of the electrical resistance is characterized in frequency and time domains, and related to the infinite system dynamics. A robust experimental realization of the system is constructed which achieves electromechanical coupling through a moving coil and magnet system. The apparatus is used to show that the band gap location and depth can be readily tuned with the circuit elements. The presented metamaterial has potential for meaningful vibroacoustic practical applications in addition to revealing fundamentally new properties of damped electrically-resonant structures.

Keywords: metametamaterials, electromechanical coupling, tunable band gap, negative impedance, metadamping

(Some figures may appear in colour only in the online journal)

1. Introduction

Metamaterials comprise a class of engineered materials which exhibit properties that are beyond those expected of normal materials, such as reflective or absorptive properties that seem to defy the conventional laws of physics imposed on bulk materials. In structural systems, metamaterials have been shown to possess remarkable vibration absorption properties stemming from their ability to exhibit band gaps, i.e. frequency regions within which wave propagation is heavily attenuated [1, 2]. Band gaps can stem from material or geometric periodicity in phononic crystals (PCs) [3–6] or from local resonances in acoustic metamaterials (AMs) [7–11]; the latter is the main focus of this study. Band gaps in AMs can be tuned by adjusting the inertial and elastic properties of the local resonators, allowing them to exhibit desirable vibration control

* Author to whom any correspondence should be addressed.

capabilities that extend to lower frequencies while using smaller geometric scales than PCs [12]. As a result, they have been recently utilized in various applications ranging from directional filtering [13, 14] and energy harvesting [15–18], to underwater sound absorption [19] and nonreciprocal systems [20, 21].

System tunability is a critical property if metamaterials are to fully realize their potential. The motivation to develop metamaterials which alter their dynamic behavior or dispersion profiles in response to changing excitations has spurred a number of efforts aiming to integrate smart transducers within metamaterial designs, including piezoelectrics [22, 23], magnetoelastic [24], and magnetorheological materials [25]. Electrically tunable metamaterials are particularly attractive due to the accessibility of electrical parameters; the wave propagation behavior can also be adjusted instantaneously, which is a significant advantage over thermally tunable metamaterials (e.g. shape memory polymers [26] and alloys [27]). This, for example, has been shown in the tunable behavior of piezoelectric wave guides [28], the auxetic behavior of piezoelectric elements [29], and the longitudinal wave control of soft dielectric elastomers [30]. Electrical band gap control has been successfully demonstrated using stiffening and softening negative impedance circuits [31] as well as negative capacitance piezoelectric shunting [32]. Using the latter, a hybrid metamaterial with negative effective mass density and tunable bending stiffness was designed [33]. Furthermore, it was experimentally shown that digital control circuits can be used to create a self-adaptive metamaterial beam with broadband flexural wave attenuation at subwavelength scales [34], most recently via synchronized switching damping on inductor dual-connected electronic networks [35]. The utility of electromechanically coupled metamaterials (EMMs) for forming both mechanical and electrical band gaps was recently demonstrated [36], albeit for undamped and very lightly damped mechanical resonators (maximum damping ratio of 2%), and in the complete absence of electrical damping.

The vast majority of analysis of locally resonant metamaterials is conducted on the undamped (lossless) version of the unit cell under consideration. Consequently, interpretation of band gaps in damped systems has remained a largely underexplored area. The presence of material damping provides a second dimension to the wave attenuation problem in the form of a temporal decay of oscillations outside band gap regions. This is typically accompanied with additional complexity in the treatment and interpretation of the dispersion equations, which inevitably makes for a challenging mathematical problem involving complex frequencies, wavenumbers, or both [37]. However, such interpretation has shed light onto an intriguing interplay between damping and local resonances which has been shown to amplify the dissipation level in a resonant metamaterial corresponding to a fixed damping amount. This ability of a locally resonant metamaterial to exhibit a superior dissipative response compared to a PC of the same damping composition is commonly referred to as *metadamping*, and was first conceptualized in simple mass-in-mass lattices [38], and later in continuous [39], non-local [40, 41], and multi-resonator metamaterials [42]. To date, the above treatment has been solely limited to mechanical damping, particularly focusing on material loss and viscous-to-viscoelastic transitions [43]. The dynamics of electrically damped local resonances will be carefully studied in this work, providing a connecting chapter for the domains of electromechanical metamaterials as well as metamaterials augmented with damped resonances.

This work presents a comprehensive theoretical and experimental analysis of an electrically-tunable AM which achieves electromechanical coupling through a moving coil and magnet system. The novel configuration has several features that render it an attractive candidate for practical vibration isolation, including low barrier-to-entry construction materials (affordable consumer grade electronics) and powerful vibration suppression capabilities. The theoretical description yields new insight into the fundamental physics of electrically-dissipative structures. The equations of motion are derived from first principles and the dispersion relations for the undamped and electrically damped system are presented. Following which, a finite system model is derived and used to investigate the various means of tuning the emergent band gap. Finally, an experimental setup is described which leverages a negative impedance converter (NIC) circuit to negate the inherent resistance in the commercial unit cell coils, and is used to demonstrate the tunability of the electrically-resonant metamaterial.

2. Electromechanical system description

2.1. Lagrangian mechanics and governing equations

An illustration of the general concept for the EMM is shown in figure 1(a). The system is composed of repeating identical unit cells which consist of a mass m and are connected to the preceding and subsequent masses via a spring of stiffness k, a dashpot of damping coefficient c, and a special, idealized, electromechanical coupling element with coefficient b which captures the interaction of a moving coil and permanent magnet coupling mechanism. The mechanical degree of freedom u_n is the position of the nth mass in the chain relative to its rest location. Each unit cell has length a which represents the lattice constant. The electromechanical coupling element itself houses the electrical degree of freedom, the charge in the nth circuit, q_n. The circuits in each electromechanical coupling element are independent and electrically isolated; the nth circuit is shown in figure 1(b). The circuit consists of an effective voltage source (which represents the voltage induced in the circuit by the electromechanical coupling), inductance L, resistance R, and capacitance C (given by the elastance, S, the inverse of capacitance). The mechanical and electrical systems are coupled through a permanent magnet which is fixed to the unit cell mass, and an electrical coil which is fixed to the previous mass in the chain such that relative motion between the two results in an induced voltage in the coil and an additional magnetic field generated by the current through the coil.

To derive the governing equations for the chain of electromechanically coupled moving-coil speakers, the models

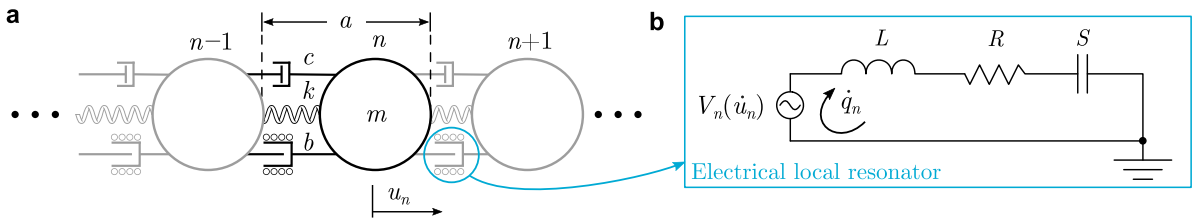

Figure 1. Proposed electromechanical metamaterial chain: (a) schematic of three unit cells in a uniform chain; each unit cell has mass m, spring stiffness k, mechanical damping c, and electromechanical coupling element with coefficient b which encompasses the electrical degree of freedom, (b) electrical resonator circuit with inductance L, resistance R, and elastance S (inverse capacitance).

given in *Mechatronics* [44] (which describe a single magnet-coil system) and current literature [45] (which describe damped, lumped, periodic structures) are referenced. The derivation adopts Lagrangian mechanics, which first requires identifying the total energy in the system. We define the generalized coordinates to be the displacements of the magnet mass u_n and the charge in the circuit coil q_n. The kinetic energy and potential energy can be expressed as:

$$T = \frac{1}{2} m \dot{u}_n^2 \tag{1a}$$

$$V = \frac{1}{2} k (u_n - u_{n-1})^2 + \frac{1}{2} k (u_n - u_{n+1})^2 + \frac{1}{2} S q_n^2. \tag{1b}$$

The magnetic energy in the nth circuit must be included as an additional term in the Lagrangian. The magnetic energy is often analyzed in terms of the magnetic coenergy, and the two terms are equivalent if the flux linkage is assumed to be linearly related to the current [46]. In this work the displacements of the mass are assumed to be small enough to maintain linearity in the springs as well as in the flux-current relationship. The magnetic coenergy W_m^* is defined in terms of the current $\dot{q}_n$ and the flux linkage λ_n as:

$$W_m^* = \int_0^{\dot{q}_n} \lambda_n \, \mathrm{d}\dot{q}_n, \tag{2}$$

where the asterisk explicitly denotes that this is a coenergy quantity. The magnetic flux linkage in the circuit is defined as the integral of the voltage with respect to time [44, 47]. The voltage generated in the circuit (from Faraday's Law) is:

$$V_{n,\text{magnet}} = b(\dot{u}_n - \dot{u}_{n-1}), \tag{3}$$

with the constant coupling coefficient defined as:

$$b = 2\,\pi N_t r_c \alpha, \tag{4}$$

where N_t and r_c are the number of turns and the radius of the wire coil and α is the permanent magnetic field flux density. The voltage from the current in the coil is:

$$V_{n,\text{current}} = L\ddot{q}_n. \tag{5}$$

As such, the magnetic flux linkage λ is the integral of the sum of the voltage from the relative motion of the coil and magnet plus the voltage from the current in the coil:

$$\lambda_n = \int (V_{n,\text{magnet}} + V_{n,\text{current}}) \, \mathrm{d}t. \tag{6}$$

Since the motion of both the previous and subsequent mass in the chain influence the coil voltage from the magnet, the flux linkage in both the nth circuit and the $(n+1)$th circuit must be considered. Alternatively, the argument can be made to consider any flux linkage which is related to either of the generalized coordinates; the result is that both λ_n and λ_{n+1} should be written, which yields:

$$\lambda_n = L\dot{q}_n + b(u_n - u_{n-1}) \tag{7a}$$

$$\lambda_{n+1} = L\dot{q}_{n+1} + b(u_{n+1} - u_n). \tag{7b}$$

Finally, the total magnetic coenergy and the dissipation function are defined as:

$$\begin{aligned} W_m^* = &\frac{1}{2} L \dot{q}_n^2 + \frac{1}{2} L \dot{q}_{n+1}^2 \\ &+ b\dot{q}_n(u_n - u_{n-1}) + b\dot{q}_{n+1}(u_{n+1} - u_n) \end{aligned} \tag{8a}$$

$$D = \frac{1}{2} c (\dot{u}_n - \dot{u}_{n-1})^2 + \frac{1}{2} c (\dot{u}_{n+1} - \dot{u}_n)^2 + \frac{1}{2} R \dot{q}_n^2, \tag{8b}$$

respectively, and the Lagrangian is defined as:

$$\mathcal{L} = T + W_m^* - V, \tag{9}$$

which has been written directly with the magnetic coenergy since it is equivalent to the magnetic energy [46, 47]. Substituting equations (1*a*), (1*b*), and (8*a*) into equation (9), the Lagrangian can be written as:

$$\begin{aligned} \mathcal{L} = &\frac{1}{2} m \dot{u}_n^2 + \frac{1}{2} L \dot{q}_n^2 + \frac{1}{2} L \dot{q}_{n+1}^2 \\ &+ b\dot{q}_n(u_n - u_{n-1}) + b\dot{q}_{n+1}(u_{n+1} - u_n) \\ &- \frac{1}{2} k (u_n - u_{n-1})^2 - \frac{1}{2} k (u_n - u_{n-1})^2 - \frac{1}{2} S q_n^2, \end{aligned} \tag{10}$$

and Largrange's equations become:

$$\frac{\mathrm{d}}{\mathrm{d}t}\frac{\partial \mathcal{L}}{\partial \dot{u}_n} + \frac{\partial D}{\partial \dot{u}_n} - \frac{\partial \mathcal{L}}{\partial u_n} = 0 \tag{11a}$$

$$\frac{\mathrm{d}}{\mathrm{d}t}\frac{\partial \mathcal{L}}{\partial \dot{q}_n} + \frac{\partial D}{\partial \dot{q}_n} - \frac{\partial \mathcal{L}}{\partial q_n} = 0. \tag{11b}$$

Evaluating the Lagrangian for both degrees of freedom yields:

$$\begin{aligned} m\ddot{u}_n + 2\,c\dot{u}_n - c(\dot{u}_{n+1} + \dot{u}_{n-1}) + 2\,ku_n \\ -k(u_{n+1} + u_{n-1}) - b\dot{q}_n + b\dot{q}_{n+1} = 0 \end{aligned} \tag{12a}$$

$$L\ddot{q}_n + R\dot{q}_n + Sq_n + b\dot{u}_n - b\dot{u}_{n-1} = 0. \tag{12b}$$

Equations (12*a*) and (12*b*) represent the set of governing equations for the two degrees of freedom of the EMM unit cell. It is worth noting that there are key differences here from previously published efforts: the equations are coupled by the damping terms, the velocity and current, and the equations of motion are asymmetric (but still Hermitian in matrix form). It is also interesting to note that that the local resonance coupling is dependent on the mechanical degree of freedom of the nth and $(n-1)$th cell, while depending on the electrical degree of freedom in the nth and $(n+1)$th cell. This is distinct from traditional fully-mechanical locally resonant systems which include no coupling between adjacent cells in the locally resonant degree of freedom [10].

2.2. Unit cell analysis

Owing to their periodic nature, several hallmark features of metamaterials can be extracted from a dispersion analysis of a single unit cell. Such analysis depicts the behavior of an infinite chain comprised of such cells connected in series, and forgoes any boundary conditions or truncation effects, but provides a commonly-used blueprint for the design of the finite system during later stages. A Bloch-wave solution of the form:

$$u_n(n,t) = \tilde{U}\,\mathrm{e}^{\mathrm{i}\mu an - \gamma t} \tag{13a}$$

$$q_n(n,t) = \tilde{Q}\,\mathrm{e}^{\mathrm{i}\mu an - \gamma t}, \tag{13b}$$

can be assumed which exploits the fact that the solution field of a periodic system is inherently periodic (i.e. a plane wave modulated by a periodic function). Here, $\tilde{U}$ and $\tilde{Q}$ are the complex wave amplitudes for the mass displacement and charge waves, respectively, μ is the wavenumber, and γ is the complex oscillation frequency. The displacement of the nth unit cell, u_n, and the charge on the associated coil, q_n, are defined at the location of the nth unit cell an (unit cell index multiplied by unit cell length) at time t. After substituting equations (13*a*) and (13*b*) into the governing equations, equations (12*a*) and (12*b*), we arrive at:

$$\mathbb{M}_B\ddot{\mathbf{x}}_B + \mathbb{C}_B\dot{\mathbf{x}}_B + \mathbb{K}_B\mathbf{x}_B = \mathbf{0}, \tag{14}$$

where

$$\begin{aligned} \mathbb{M}_B &= \begin{bmatrix} m & 0 \\ 0 & L \end{bmatrix}, \\ \mathbb{C}_B &= \begin{bmatrix} 2\,c(1-\cos\mu a) & b(\mathrm{e}^{\mathrm{i}\mu a}-1) \\ b(1-\mathrm{e}^{-\mathrm{i}\mu a}) & R \end{bmatrix}, \\ \mathbb{K}_B &= \begin{bmatrix} 2k(1-\cos\mu a) & 0 \\ 0 & S \end{bmatrix}, \\ \mathbf{x}_B &= \begin{Bmatrix} \tilde{U}\mathrm{e}^{\gamma t} \\ \tilde{Q}\mathrm{e}^{\gamma t} \end{Bmatrix} \end{aligned} \tag{15}$$

where the subscript B denotes the Bloch solution for the infinite chain case, with matrix variables written in blackboard-bold font and vectors in roman bold font, and $\mathbf{0}$ is the zero vector. To determine the relationship between the wavenumber μ and the oscillation frequency γ, this matrix differential equation can be recast into an eigenvalue problem by applying a state-space transformation [37]. First, let $\mathbf{y}_B = \{\mathbf{x}_B,\ \dot{\mathbf{x}}_B\}^{\mathrm{T}}$, and define $\mathbf{y}_B = \tilde{\mathbf{Y}}_B\mathrm{e}^{\gamma t}$, where $\tilde{\mathbf{Y}}_B = \{\tilde{U},\ \tilde{Q},\ \gamma\tilde{U},\ \gamma\tilde{Q}\}^{\mathrm{T}}$, such that the matrix equation above can be written as:

$$\left(\begin{bmatrix} \mathbb{O} & \mathbb{M}_B \\ \mathbb{M}_B & \mathbb{O} \end{bmatrix}\gamma + \begin{bmatrix} \mathbb{K}_B & \mathbb{C}_B \\ \mathbb{O} & -\mathbb{M}_B \end{bmatrix}\right)\tilde{\mathbf{Y}}_B = \mathbf{0}, \tag{16}$$

where $\mathbb{O}$ is a 2×2 zero matrix.

2.3. Undamped dispersion analysis

The eigenvalues can be found analytically for the undamped cases, i.e. setting $c=0$ and $R=0$ in equation (15) and solving for the values of γ that satisfy equation (16) while specifying explicitly $\gamma = \mathrm{i}\omega$, where ω is the angular frequency. The polynomial that defines the eigenvalues for the undamped, infinite length, electromechanically coupled chain evaluates to:

$$\begin{aligned} mL\gamma^4 + \gamma^2\,\big[2\,kL(1-\cos\mu a) \\ + 2b^2(1-\cos\mu a) + Sm\big] \\ + 2\,kS(1-\cos\mu a) = 0. \end{aligned} \tag{17}$$

The above equation can be cast in a normalized form for better interpretation. By defining:

$$\omega_m^2 = \frac{k}{m}, \quad \omega_e^2 = \frac{S}{L}, \quad \beta^2 = \frac{b^2}{mL}, \tag{18}$$

and the unitless parameters:

$$\Omega = \frac{\omega}{\omega_m}, \quad E = \frac{\omega_e}{\omega_m}, \quad B = \frac{\beta}{\omega_m}, \tag{19}$$

equation (17) can be rewritten as:

$$\begin{aligned} \Omega^4 - \Omega^2\left[2(1-\cos\mu a) + 2B^2(1-\cos\mu a) + E^2\right] \\ + 2\,E(1-\cos\mu a) = 0, \end{aligned} \tag{20}$$

where μa denotes the dimensionless wavenumber. The roots of this expression for a given μa define the dispersion bands for this unit cell. In practice, one can either specify a real μa and solve for Ω, or specify real Ω and solve for a complex μa. The

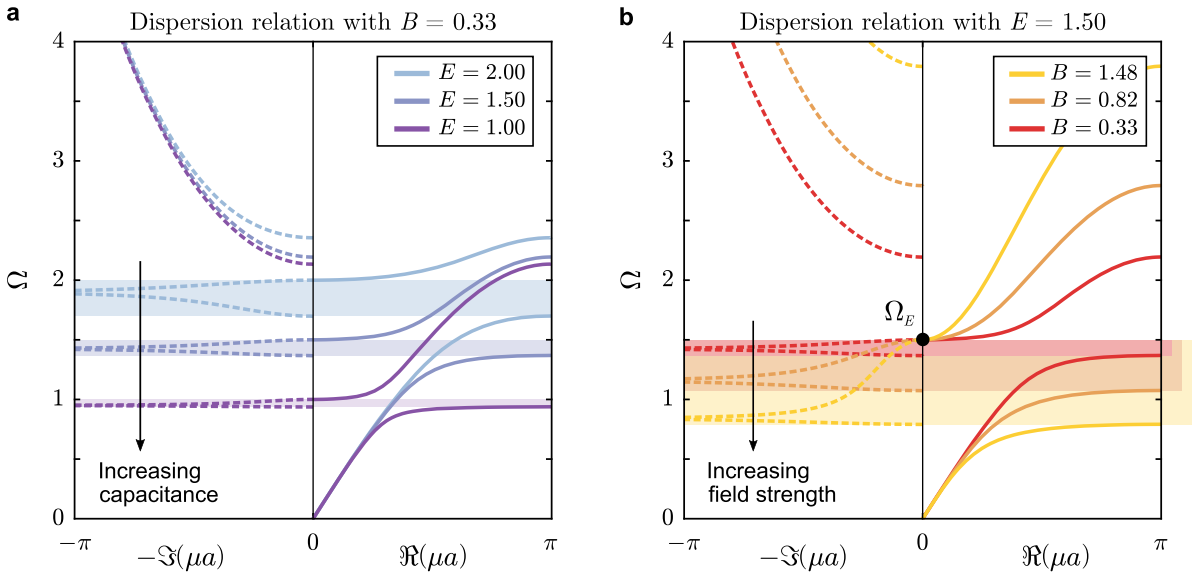

Figure 2. Dispersion relation for an infinite EMM chain with no damping: (a) band gap shift as external capacitance is varied and (b) band gap growth as magnetic field strength is increased.

latter is known as the driven-wave approach since the incident wave frequency is dictated as an input to the problem [6, 39]. In a completely undamped chain with no energy dissipation over time, we expect a purely real oscillation frequency. Therefore, we specify a real Ω and solve for (generally complex but not always) μa. Henceforth, we use the symbols $\Re(\cdot)$ and $\Im(\cdot)$ to indicate the real and imaginary parts of a given argument, respectively. In this scenario, and in the absence of temporal attenuation due to the lack of material or electrical damping, a non-zero imaginary part of the wavenumber indicates a spatial attenuation mechanism which is indicative of a band gap spanning the frequency range within which $\Im(\mu a)$ exists, whereas $\Re(\mu a)$ plot the dispersion bands for any frequency Ω outside such gaps. Solving equation (20) for μa yields:

$$\cos\,\mu a = \frac{\Omega^4 - \Omega^2(2+2B^2+E^2)+2\,E^2}{-2\Omega^2(1+B^2)+2E^2}, \tag{21}$$

which leads to a specific frequency where the wavenumber is undefined, i.e. $\cos\mu a = \infty$, by defining the asymptote frequency:

$$\Omega_A = \sqrt{\frac{E^2}{1+B^2}} = \sqrt{\frac{mS}{kL+b^2}}, \tag{22}$$

where Ω_A denotes the frequency of maximum attenuation within the band gap. The lower limit of the band gap can be computed by solving for the frequency Ω_L where the wavenumber is equal to π, i.e. $\cos\mu a = -1$ [48], to find:

$$\Omega_L = \left(P - \sqrt{P^2 - 4E^2}\right)^{\frac{1}{2}}, \tag{23}$$

where $P = 2(1+B^2+E^2/4)$. As will be discussed shortly, the band gap emerging in this system is a local resonance band gap, which is uniquely identified with a π phase shift in μa on both ends of the gap. As such, the band gap closes when $\mu = 0$. Solving equation (21) for $\cos\,\mu a = 1$, we get:

$$\Omega_E = E, \tag{24}$$

as the upper limit of the band gap. For completeness, we also define the frequency of the upper limit of the acoustic mode, Ω_S, which indicates the starting frequency of the stop band, i.e. an unbounded band gap which constitutes the end of the dispersion profile of any lumped-parameter system [2].

Figure 2(a) shows the dispersion bands for varying external capacitance. The bands are computed by sweeping the frequency Ω over a range of real values in equation (20) and solving for the complex wavenumber μa. Note that the dispersion relation polynomial, equation (20), was found with no mechanical or electrical damping, i.e. $c = 0$ and $R = 0$, but still accounts for the electromechanical coupling in the system. The electrical circuit resonance frequency is shown to be the upper limit of the band gap, and thus the wave attenuation region can be controlled by varying the electrical capacitance in the external circuit of each unit cell. Increasing the capacitance leads to a lower electrical resonance frequency, E, and consequently the band gap upper limit Ω_E moves down on the frequency axis. Figure 2(b) shows the impact of varying the magnetic field strength coefficient, b, (represented in terms of the non-dimensional magnetic parameter B) on the dispersion bands. The upper limit of the band gap, Ω_E, does not depend on the magnetic coupling coefficient b and so it does not change. However, the asymptote frequency Ω_A does depend on b: increasing the magnetic field strength (defined as α but tuned using b for simplicity) decreases the magnitude of the asymptote frequency (and lower limit Ω_L), therefore increasing the width of the band gap. Note this must not change the coil parameters, otherwise L and consequently E would change.

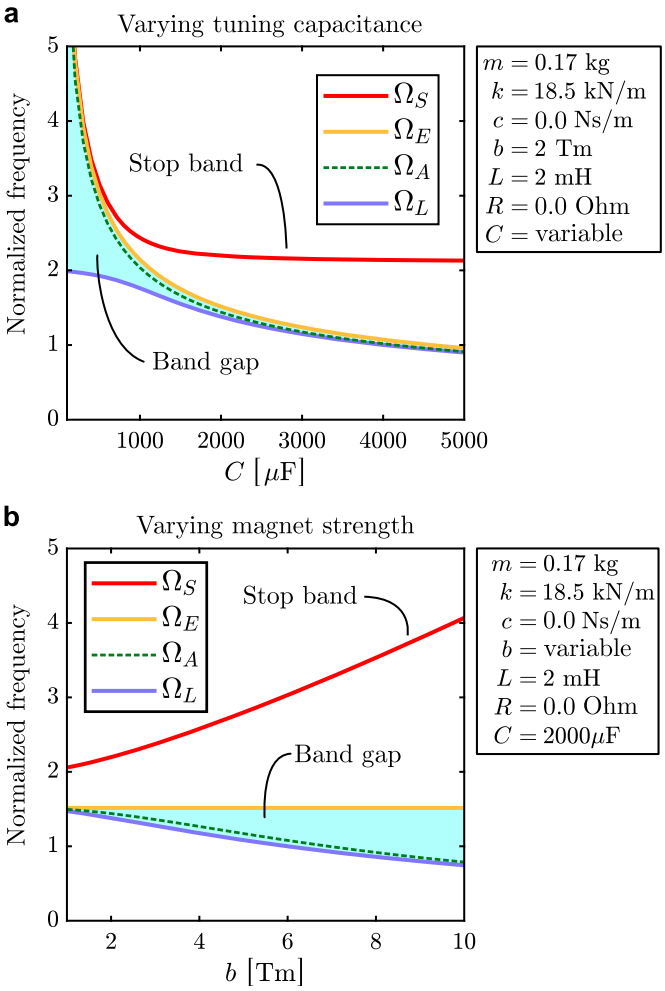

Figure 3. Evolution of key band gap parameters as (a) circuit capacitance and (b) magnet strength are increased. The frequency of the stop band Ω_S above which no waves will propagate, upper band gap limit Ω_E, asymptote frequency (maximum attenuation) Ω_A, and lower band gap limit Ω_L as predicted by the dispersion relation are graphed as functions of a single variable system parameter as indicated by the tables adjacent to each plot.

The tunability of the electrical local resonance band gap is summarized in figure 3. Four key parameters of the dispersion curves are computed as either the external circuit capacitance or the magnet strength is varied. The key parameters are the frequency at which the stop band begins, Ω_S, the upper and lower band gap limits Ω_E and Ω_L, respectively, and the frequency of maximum attenuation Ω_A. A set of system parameters are chosen in order to provide some idea for system design as well as place this figure in context with the experimental results presented in later sections. In figure 3(a), the capacitance is varied while the other parameters are held constant. The undamped band gap region is shaded for clarity. In figure 3(b) the magnetic field strength is varied while the other parameters are held constant. The fixed location of Ω_E in figure 3(b) highlights the independence of the electrical resonance frequency from the magnetic field strength parameter b, while the significant variation in both Ω_A and Ω_L indicates the utility of selecting a magnetic field strength based on system performance requirements.

2.4. Damped dispersion and electrical metadamping

The eigenvalue problem which dictates the relationship between the temporal oscillation frequency and the (complex) spatial wavenumber was investigated analytically in the previous section for a completely undamped case. It is of significant interest to examine the impact of electrical damping on the EMM chain for several reasons: first, the electrical resistance of each unit cell can be easily tuned in a practical setting and, second, the effects of damping within a locally resonant metamaterial have been an intriguing topic of investigation in several recently published efforts (a comprehensive review of such efforts can be found in [41]). The following section sheds insight into the wave dispersion mechanics of EMMs comprising electrically damped resonances and discusses the notion of *electrical metadamping*; a mechanism to achieve a desirable dissipative behavior (reminiscent of *mechanical metadamping* systems) with tuning capabilities given its sole dependence on easily-changeable resistive elements.

The eigenvalues of the damped dispersion relation can be found numerically using equation (16). The damped natural frequency, Ω_d, and the damping ratio, ζ_d, are computed as:

$$\Omega_d = \Im(\gamma(\mu a))/\omega_m \tag{25a}$$

$$\zeta_d = -\frac{\Re(\gamma(\mu a))}{|\gamma(\mu a)|}, \tag{25b}$$

where the eigenvalues $\gamma(\mu a)$ are explicitly functions of the real wavenumber μa [39]. If a computational tool (e.g. MATLAB) is used to compute the eigenvalues in an iterative manner (i.e. sweeping through a μa vector in a `for` loop), the algorithm must maintain the order of the eigenvalues with their respective mode shapes in order to have a meaningful result. It is likely that the solver will return the eigenvalues in different vector indices if left to chance. To track the modes, the modal assurance criterion is adopted, which is defined as [49]:

$$M(a,\ b) = \frac{\left|\mathbf{v}_a^{\mathrm{T}}\mathbf{v}_b\right|^2}{\left(\mathbf{v}_a^{\mathrm{T}}\mathbf{v}_a\right)\left(\mathbf{v}_b^{\mathrm{T}}\mathbf{v}_b\right)}, \tag{26}$$

and is essentially a normalized dot product between the eigenvectors $\mathbf{v}_a$ and $\mathbf{v}_b$. If the eigenvectors are the same, then $M(a,a) = 1$. If they are orthogonal, then $M(a,b) = 0$. To track the system eigenvalues through multiple iterations (as the system parameters are varied), we compute the eigenvalues of the state matrix, then arrange them in an order that minimizes $M(a,b)$ when compared to the previous iteration. This sorting step takes place for each new wavenumber value that is substituted into the mass, stiffness and damping matrices when computing the dispersion curves. Figure 4 shows the variation of Ω_d and ζ_d with μa, as well as ζ_d as a function of Ω_d, for different value of the electrical resistance, R. Given the focus on electrical damping, we set $c = 0$ for simplicity. Figure 4(a)

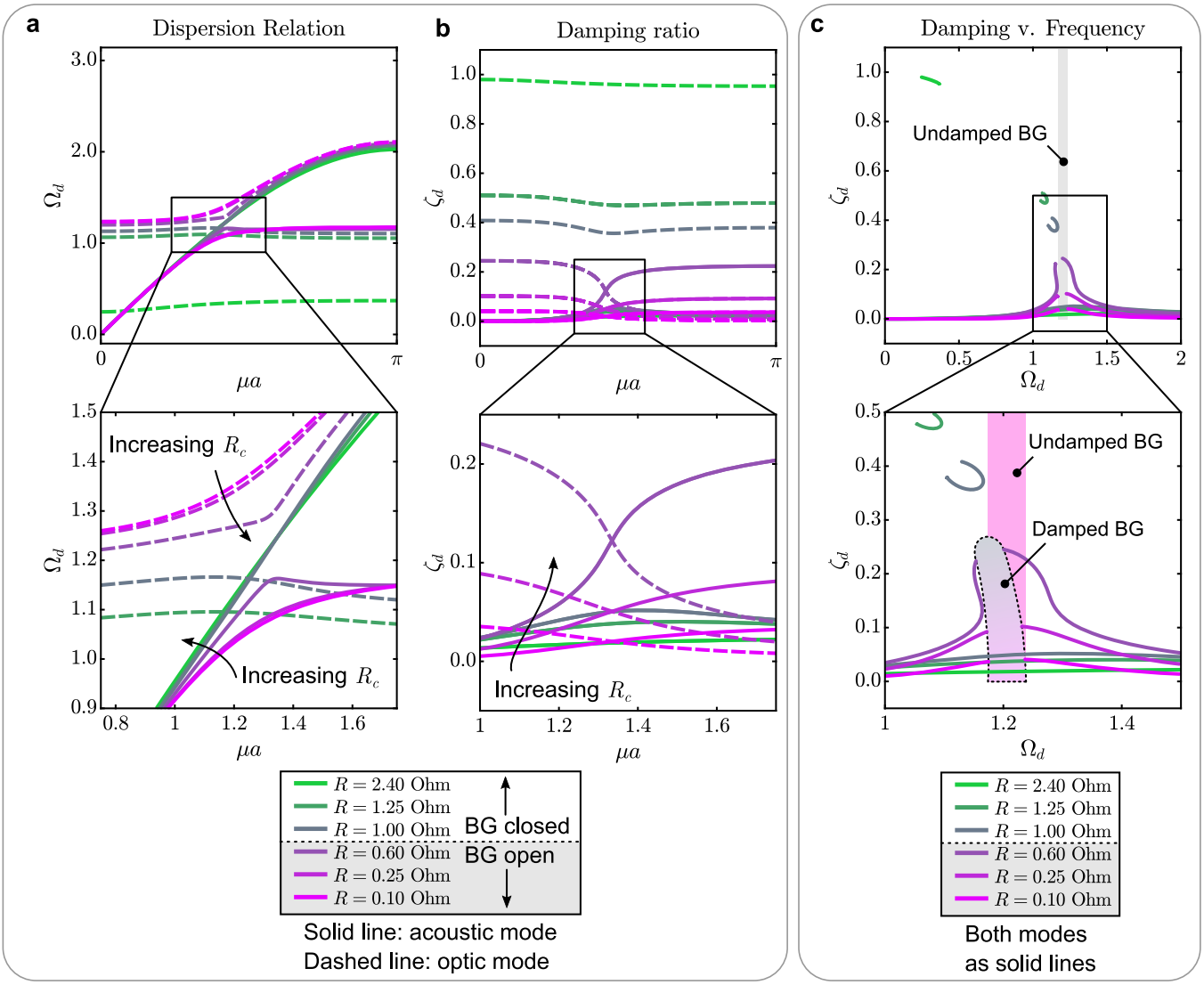

Figure 4. Dispersion relation for electrically damped, mechanically undamped ($c = 0$), infinite chain of electromechanically coupled metamaterial cells: (a) variation in dispersion curves as electrical resistance is decreased, (b) variation in damping ratio, (c) damping ratio as a function of damped frequency.

depicts the damped dispersion behavior, i.e. the damped oscillation frequency Ω_d against μa. Figure 4(b) provides the corresponding variation of the damping ratio ζ_d of the infinite EMM chain with μa. In figures 4(a) and (b), solid lines indicate the acoustic mode (branch), and the dashed lines indicate the optic mode (branch) of the metamaterial. The close-ups highlight the behavior of the branches in the vicinity of the electrical local resonance band gap region, which reveal a narrowing band gap with an increasing electrical resistance R. Furthermore, the analysis shows that the gap ultimately closes beyond a critical R value which initiates a branch crossing (similar to the branch overtaking phenomenon described in [41] for mechanically damped metamaterials). Figure 4(c) shows the damping ratio graphed as a function of the damped frequency [39], and signals a unique and potentially useful feature of damped locally resonant structures: the damping ratio is unchanged at low oscillation frequencies and relatively unaffected at high frequencies, but in the region surrounding the band gap the damping ratio can be increased substantially via a fine tuning of the electrical resistance R. The lightly damped case $R = 0.10$ Ohm shows a band gap (vertical break in the close-up inset of figure 4(c) where there is no damping ratio because the damped frequency is undefined; as the electrical resistance increases, the band gap remains (i.e. for $R = 0.60$ Ohm) and the damping ratio increases from roughly 0.05 to a maximum of $\zeta_d = 0.25$ immediately before and after the band gap. The shaded region labeled 'Damped BG' illustrates the change in band gap width and location, which is an inevitable trade-off of the resistance increase. As the electrical resistance is increased to $R = 1.00$ Ohm and above (henceforth referred to as the high resistance regime), the band gap closes and the damping ratio is significantly reduced. However, a small region near the frequency where the band gap would exist breaks off and continues to follow the trend of increased damping ratio and decreasing frequency for $R = 1.00$ Ohm and above, as shown in figure 4(c). Although the band gap

is closed and the spatial attenuation is not expected along the length of the EMM chain, the temporal damping ratio is still controlled by the electrical resistance within this regime. In practice, it is difficult to make use of this parabolic satellite region because: (a) it spans an increasingly narrow frequency range which must be directly excited, and (b) targeting the highly damped mode which corresponds to the satellite region also necessarily targets the underdamped mode as well. However, the metadamping for lower resistances remains a powerful tool which will be explored further for a finite system in the following sections.

3. Dynamics of the finite metamaterial

3.1. Finite EMM model

Consider a chain of N EMM unit cells. The system parameters are the unit cell mass m, spring stiffness k, damping constant c, coil inductance L_c, capacitance C_c or elastance $S_c = 1/C_c$, resistance R_c, and electromechanical coupling factor b as described earlier. The mass, damping, and stiffness matrices, $\mathbb{M}$, $\mathbb{C}$ and $\mathbb{K}$, respectively, can be constructed from the governing equations [50]. The governing equations for the finite system can be written in matrix form as:

$$\mathbb{M}\ddot{\mathbf{x}} + \mathbb{C}\dot{\mathbf{x}} + \mathbb{K}\mathbf{x} = \mathbf{F}, \tag{27}$$

where the vector $\mathbf{x}$ is:

$$\mathbf{x} = \{u_1,\ q_1,\ u_2,\ q_2,\ \ldots\ u_N,\ q_N\}^{\mathrm{T}}, \tag{28}$$

with u_n being the displacement of the nth unit cell mass and q_n being the charge on the nth coil, and the input vector is:

$$\mathbf{F} = \{f_0(t),\ 0,\ 0,\ \ldots\ 0,\ 0\}^{\mathrm{T}}, \tag{29}$$

where the force acting on the first cell, f_0, is a harmonic function of time representing an incident excitation at one end of the EMM chain.

Another state-space realization is adopted for the finite chain case by defining the new state vector $\mathbf{z} = \{\mathbf{x},\ \dot{\mathbf{x}}\}^{\mathrm{T}}$ and the new output vector (i.e. states that are available for measurement) $\mathbf{y}$ so that equation (27) can be written as:

$$\dot{\mathbf{z}} = \mathbb{A}_s\mathbf{z} + \mathbf{B}_s f_0 \tag{30a}$$

$$\mathbf{y} = \mathbb{C}_s\mathbf{z} + \mathbf{D}_s f_0, \tag{30b}$$

The state matrix $\mathbb{A}_s$ and input matrix $\mathbf{B}_s$ define the system dynamics, and the output matrix $\mathbb{C}_s$ and direct feedforward matrix $\mathbf{D}_s$ define the states that are available for measurement. In the present case, the output states are the position of the first mass and the last mass in the chain. The system is therefore represented by:

$$\begin{aligned}
\mathbb{A}_s &= \begin{bmatrix} \mathbb{O} & \mathbb{M} \\ \mathbb{M} & \mathbb{O} \end{bmatrix}^{-1} \begin{bmatrix} -\mathbb{K} & -\mathbb{C} \\ \mathbb{O} & \mathbb{M} \end{bmatrix}, \\
\mathbf{B}_s &= \begin{bmatrix} \mathbb{O} & \mathbb{M} \\ \mathbb{M} & \mathbb{O} \end{bmatrix}^{-1} \begin{Bmatrix} \mathbf{F} \\ 0 \end{Bmatrix}, \\
\mathbb{C}_s &= \begin{bmatrix} 1 & \ldots & 0 & \ldots & 0 \\ 0 & \ldots & 1 & \ldots & 0 \end{bmatrix}, \\
\mathbf{D}_s &= \begin{bmatrix} 0 \\ 0 \end{bmatrix},
\end{aligned} \tag{31}$$

where $\mathbb{C}_s$ is zero except elements $(1,1)$ and $(2, 2N-1)$. The output vector, written explicitly in terms of the EMM chain degrees of freedom variables, is $\mathbf{y} = \{u_1,\ u_N\}^{\mathrm{T}}$. Note that the position of the first mass is $u_1 = x_1 = z_1$, the first element of the vector $\mathbf{x}$, and the position of the last mass is $u_N = x_{2N-1} = z_{2N-1}$, the second-to-last element of the vector $\mathbf{x}$ (the charge for that unit cell is the last element). This state space realization can be used to find the transfer functions between the output states and the input force applied to the first cell. The transfer function is traditionally written in the Laplace domain. Taking the Laplace transform of equations (30*a*) and (30*b*) and solving for $\mathbf{y}$ yields:

$$\mathbf{y}(s) = \mathbb{C}_s\left(s\mathbb{I} - \mathbb{A}_s\right)^{-1}\mathbf{B}_s f(s), \tag{32}$$

where s is the Laplace variable. This relationship readily provides two (in this case) transfer functions after dividing by the scalar Laplace domain forcing function:

$$G_1(s) = \frac{u_1}{f_0} = \frac{n_1(s)}{d(s)} \tag{33a}$$

$$G_N(s) = \frac{u_N}{f_0} = \frac{n_N(s)}{d(s)}, \tag{33b}$$

where each transfer function is a ratio of polynomials, n_1, n_2, and d, expressed in terms of the Laplace variable s; the transfer functions have the same denominator. To find the end-to-end transfer function, which is physically relevant for vibration isolation applications, G_N/G_1 is evaluated to find:

$$G_{N,1}(s) = \frac{n_N(s)}{n_1(s)}, \tag{34}$$

which defines the transfer function between the motion of the first mass in the chain and the motion of the last mass. For vibration isolation, the steady-state response is commonly extracted from Laplace transfer functions [10], which yields the frequency response function:

$$H_{N,1}(\omega) = G_{N,1}(\mathrm{i}\omega). \tag{35}$$

The end-to-end frequency response functions, $H_{N,1}$, are shown in figure 5 for varying system parameters. Figure 5(a)

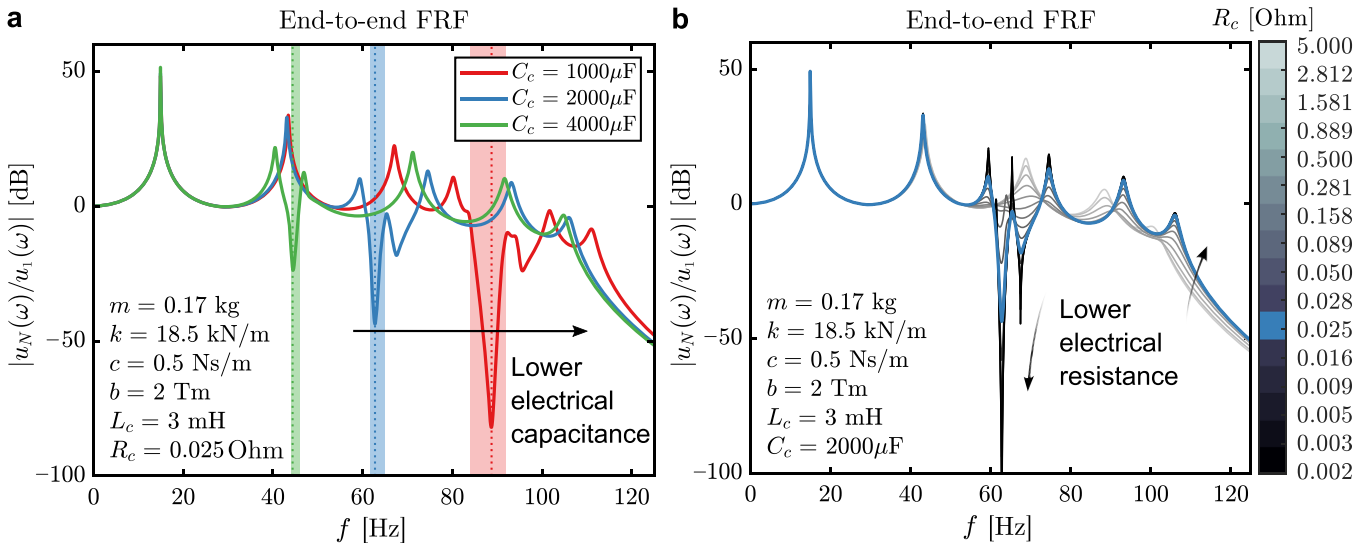

Figure 5. Acceleration frequency response functions for varying electrical parameters: (a) varying electrical resonance frequency by changing tuning capacitance places band gap at chosen frequency, and (b) varying tuning resistance changes depth of attenuation.

shows the frequency response function in dB for a given set of system parameters and three different capacitor values. The total series resistance in the electrical circuit is set to $R_c = 0.025$ Ohm in figure 5(a). In figure 5(b) the capacitance is set to $C_c = 2000$ μF and the resistance is varied. When the external circuit capacitance is changed, the location of the zero (or collection of zeros) in the frequency response function, i.e. the band gap, shifts according to the change in resonance frequency of the locally resonant electrical system. The frequency of maximum attenuation, $\omega_A = \Omega_A \omega_m$, as predicted by the dispersion relation, is represented by a dotted line for each capacitance value. Note that the region of maximum attenuation is not located at the natural frequency of the local resonators, ω_e, but instead the upper limit of the band gap is ω_e. In figure 5(b), the impact of increasing damping within the local resonance system is shown: with high damping, there is no local resonance effect and the frequency response function resembles that of a uniform chain of spring-masses. As the electrical damping is decreased, the current in the coil increases and as such the magnetic force between the coil and magnet becomes relevant which results in a variation in the end to end acceleration frequency response function. The finite system frequency response functions demonstrate the utility of the EMM system. In most published experimental efforts, tuning the band gap location is difficult and requires sophisticated (or expensive) equipment. With the EMM as described, the band gap can be placed at any frequency with the appropriate selection of the tuning circuit inductance and capacitance. Further, the band gap can be completely suppressed (i.e. the structure behaves as a traditional lumped mechanical system) or exaggerated by changing the resistance in the tuning circuit. This level of control, achievable through electrical switches and potentiometers, is unprecedented in its accessibility and versatility.

The end-to-end frequency response functions provide valuable information for steady-state operation of the EMM chain, but time-domain simulations lend significant insight into the system dynamics. The frequency response function under a given force is also of significant interest depending on the application. The displacement-force FRF is:

$$H_{N,f}(\omega) = G_N(\mathrm{i}\omega). \tag{36}$$

The displacement–force FRF is shown in figure 6(a) for a range of low-magnitude resistance values. This FRF is similar to figure 5(b) but spans a narrower range of resistances such that the band gap is open for every case. The zoomed view in figure 6(c) highlights two important factors that are dependent on the electrical resistance: band gap depth, or degree of attenuation, and the amplitude of the pre-band gap (pre-BG) resonance. As the resistance is increased from 0.01 Ohm to 0.60 Ohm, the band gap becomes shallower and the amplitude of the pre-BG resonance decreases as well. Both of these observations perfectly align with the infinite chain damped dispersion analysis summarized in figure 4(c). The undamped band gap region (as predicted by the dispersion relation) is highlighted in the FRF charts. For confirmation, figure 6(b) shows the damping ratio as a function of frequency for the same resistance values, and also highlights the evolution of the damped band gap. In addition to the infinite chain analysis and the corresponding frequency response of the finite realization, the EMM's response in the time-domain is investigated via two distinct Gaussian pulse excitations that cater to different narrow frequency regions. The EMM's response is shown in figures 6(d) and (e). The excitation signals are shown in the first column of the same subfigures. The frequency content of the excitation signal is shown on the right-vertical axis of figure 6(a). Each pulse is defined by:

$$g_{1,2}(t) = \Re\left(\mathrm{e}^{-(t-t_0)^2/(2\sigma_c^2)+\mathrm{i}2\pi f_c(t-t_0)}\right), \tag{37}$$

where the center frequencies, f_c, are 56.0 Hz and 63.3 Hz, and the standard deviations σ_c are 0.35 and 0.5 for g_1 and g_2, respectively. The excitation g_1 (Excitation A) is chosen to

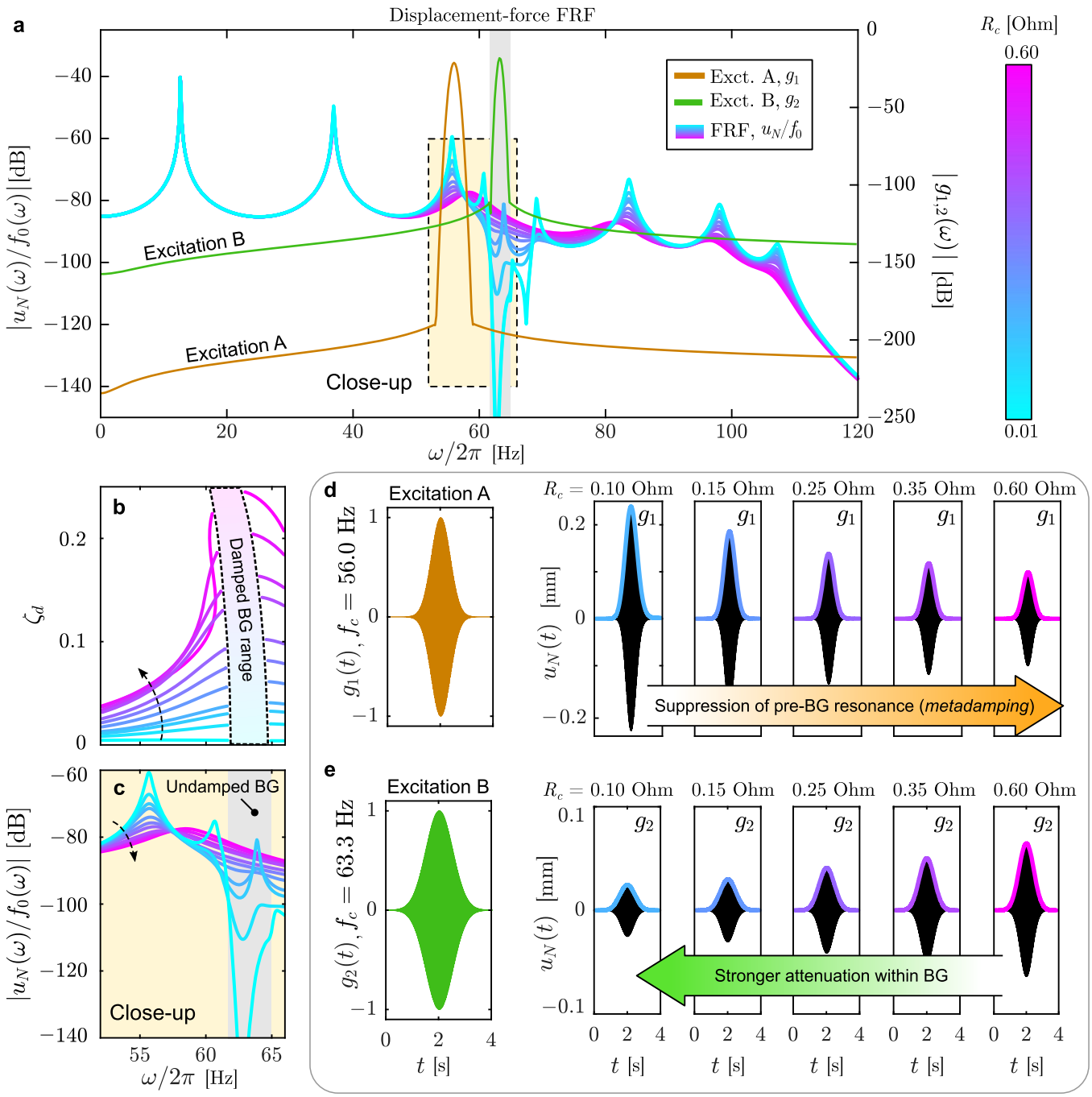

Figure 6. Finite system end-mass displacement over input force transfer function with impact of varying electrical resistance on time-domain response: (a) frequency response function for displacement of end mass relative to input force for low resistance values (left vertical axis) and two narrow-band excitation pulses (right vertical axis), (b) evolution of damping ratio with band gap for varying electrical resistance, (c) zoomed view of displacement/force FRF with undamped band gap prediction, (d) time-domain excitation A, $g_1(t)$ [N], input and time-domain simulation results (whole top row) for increasing electrical resistance which causes reduction in amplitude for frequency range just before band gap, and (e) excitation B, $g_2(t)$ [N], with time-domain simulation results for increasing resistance which demonstrate stronger attenuation within band gap at lower resistance.

excite the pre-BG resonance, and g_2 (Excitation B) has narrower bandwidth and is centered around the band gap. The upper row of time domain responses, figure 6(d), shows the excitation which targets the resonance just before the band gap and the system response for varying electrical resistance. Initially, with very low resistance, the response of the last mass in the chain has relatively large amplitude; as the resistance is increased, the response amplitude decreases and the settling time grows shorter (the system reaches $u_N = 0$ in less time with higher electrical resistance in this regime). This is directly attributed to the electrical metadamping phenomenon which causes the frequencies immediately above and below the band gap to exhibit significantly higher temporal damping. In the second row of charts, Excitation B, which is centered within

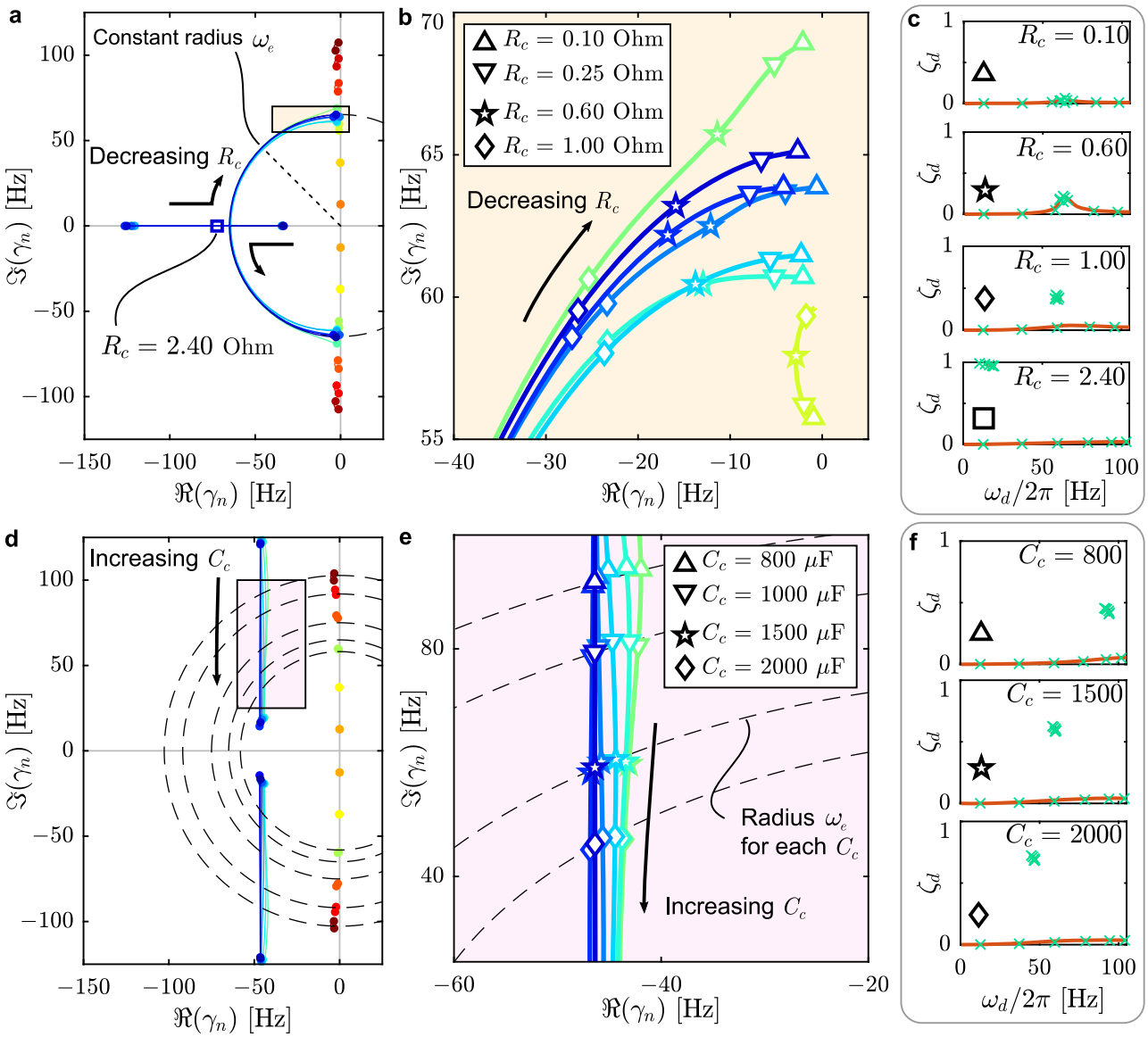

Figure 7. Evolution of state-matrix complex eigenvalues for varying electrical parameters; each eigenvalue is assigned one color, markers indicate electrical parameter value of interest: (a) with decreasing electrical resistance, one subset of eigenvalues start on real axis and break out to follow (roughly) circular path of radius $\omega_e/2\pi$, (b) zoomed view near imaginary axis and (c) damping ratio graphed against frequency which shows one group of eigenvalues with very high damping ratio at high resistance corresponding to the subset which lies on or near the real axis for that R_c value; (d) path of eigenvalues for constant resistance and varying capacitance, dashed circular lines have radius of each electrical resonant frequency, (e) zoomed view shows subset of eigenvalues lies at distance $\omega_e/2\pi$ from origin and moves as capacitance is varied, (f) plot of damping ratio vs. frequency show subset of eigenvalues that are influenced by electrical parameters moves primarily horizontally for increasing capacitance which is shown via the angle of the eigenvalue from the real axis in the complex plane.

the band gap, shows the opposite trend in response amplitude. As the electrical resistance is increased, the impact of the local resonance has less impact on the system dynamics within the band gap region and the response amplitude grows (the settling time remains the same).

To further characterize the behavior of the EMM chain under varying electrical parameters, the eigenvalues of the state matrix $\mathbb{A}_s$ are graphed in the complex plane. From the definition of the transfer functions in equation (32), the eigenvalues can be interpreted as the roots of the polynomial $d(s)$, sometimes referred to as the system 'poles.' The state matrix eigenvalues, defined as γ_n for $n = [1, 2, \ldots, 4N-1, 4N]$ describe the system dynamics independent of the output state variable configuration. The set of γ_n are computed for a range of electrical resistance values and graphed with the real part on the horizontal axis and the imaginary part on the vertical axis in figure 7(a). The eigenvalues generally fall into two distinct groups: one group remains very close to the imaginary axis regardless of the electrical resistance, and the other group shows significant variation in both real and imaginary parts as the electrical resistance is changed. In this chart the real part of the eigenvalue represents a temporal damping effect: any γ_n with a large magnitude real value (i.e. far to the left in figure 7(a)) will be heavily damped out, and a γ_n (or conjugate

pair of γ_n) with zero real part will be undamped. The eigenvalues which are influenced by the electrical resistance all start on the real axis, which indicates there is no oscillatory motion for these poles. As the resistance is decreased below $R_c = 2.4$ Ohm (exact value depends on the eigenvalue pair in question) the eigenvalues collide on the real axis and break out into the complex plane with a non-zero imaginary component. As the resistance is decreased further, these poles trace a (roughly) circular path around the origin. The close-up view in figure 7(b) shows the behavior of the eigenvalues for low resistance values. Pointed markers indicate the location of each eigenvalue at some specific resistance value. The damping ratio as a function of frequency is shown in the series of charts in figure 7(c), with a solid line from the dispersion relation prediction and an $\times$ marker for the value computed with the finite system poles. In the uppermost chart of figure 7(c), with the lowest resistance, all the eigenvalues lie near the imaginary axis which corresponds to low damping ratio as expected. As the resistance is increased, such as the $R_c = 0.60$ Ohm case, one group of eigenvalues moves away from the imaginary axis and the damping ratio increases, but only at the frequencies (vertical coordinate in figure 7(b) and horizontal coordinate in figure 7(c)) near that group of eigenvalues. At some resistance value (roughly 0.65 Ohm), even though that group of eigenvalues continues on their path toward higher damping ratio (greater magnitude real part) and lower frequency (smaller magnitude imaginary part) they are too far from the imaginary axis to be relevant to the system response, and become a satellite group as observed in figure 4.

The impact of varying the circuit capacitance is shown in figure 7(d) and with a zoom view in figure 7(e). Changing the electrical capacitance directly causes a change in the electrical resonant frequency (inverse square root relationship). The closely packed group of eigenvalues that are influenced by the electrical parameters, therefore, moves vertically in the complex plane and each new capacitance value can be tied to a circular trace around the origin on which the eigenvalues all lie (roughly). The imaginary part of this group of poles dictates the frequency at which the band gap is located, and the angle they make with the real axis indicates the depth of the band gap. This explains the decreasing magnitude of attenuation as the capacitance was increased in figure 5(a): as the capacitance is increased, these eigenvalues move to lower frequencies but their angle with respect to the positive real axis also increases, and as such their impact is lower. The same effect is demonstrated in the damping ratio charts in figure 7(f). At low capacitance, the satellite group of eigenvalues has relatively low damping ratio, but as the capacitance is increased the damping ratio is as well.

3.2. Summary of theoretical EMM results

The results presented thus far can be summarized by considering the complex plane eigenvalue plots as being a generalized representation of the behavior of the finite EMM system under varying electrical parameters. The detailed plots of figures 2 through 6 show important performance characteristics from the dispersion relations and frequency response function and provide a framework for making specific design decisions or dissecting system strengths and limitations. For example, the band gap ending frequency can be directly controlled by the electrical resonance frequency as shown in the dispersion diagrams and confirmed by the end-to-end FRFs, and the band gap width can be set by choosing the permanent magnet field strength. The attenuation depth can be tuned by varying the resistance. Importantly, the time domain results of figure 6 highlight the need for understanding the impact of damping with respect to the anticipated excitation frequencies. The high-level performance of the system is captured in the complex plane charts, albeit with less detail (or at least less explicitly obvious detail). The damping ratio—which determines that important time-domain response—can be computed from the location of the group of satellite poles. The undamped band gap frequency can be seen in the radial distance of that satellite group from the origin, and the attenuation depth is correlated with the horizontal location of that group of poles. In a sense, representing the EMM system in the abstract, generalized framework of the poles in the complex plane opens up many new avenues for leveraging classical control strategies within the context of metamaterials. Significantly more research is required to firmly ground this class of system within the context of control theory, or to apply such techniques in a reliable and predictable way (pole placement controller design in the context of the locally resonant system as a feedback controller, for example) but the connections between the familiar representation of FRF performance, new band structures which are increasingly important in recent literature such as damping ratio as a function of frequency, and the complex plane representation are certainly strong enough to warrant such future investigations.

4. Experimental performance of the EMM

One of the most attractive features of the proposed EMM chain is the accessibility of construction using commonly available materials without sacrificing system performance. The electromechanical coupling as presented in the previous sections is readily achieved through a moving coil and magnet system; such systems are common in audio applications and can be purchased at low cost and constructed into an EMM chain with few additional parts. Figure 8(a) shows a block diagram representation of the requirements of the EMM unit cell. The mechanical system is represented by the key parameters m, c, and k in the upper block as a multi-input multi-output block. The mechanical system has inputs for mechanical force and a magnetic force, and outputs for the mass acceleration and velocity. The mechanical system is coupled to an electrical block represented by L, R, and C which has an input of voltage and output of current. The two subsystems are tied together through the electromechanical coupling coefficient b.

4.1. DAEX unit cell

The experimental unit cell and accompanying tuning circuit are shown in figure 8. The unit cell is a commonly available

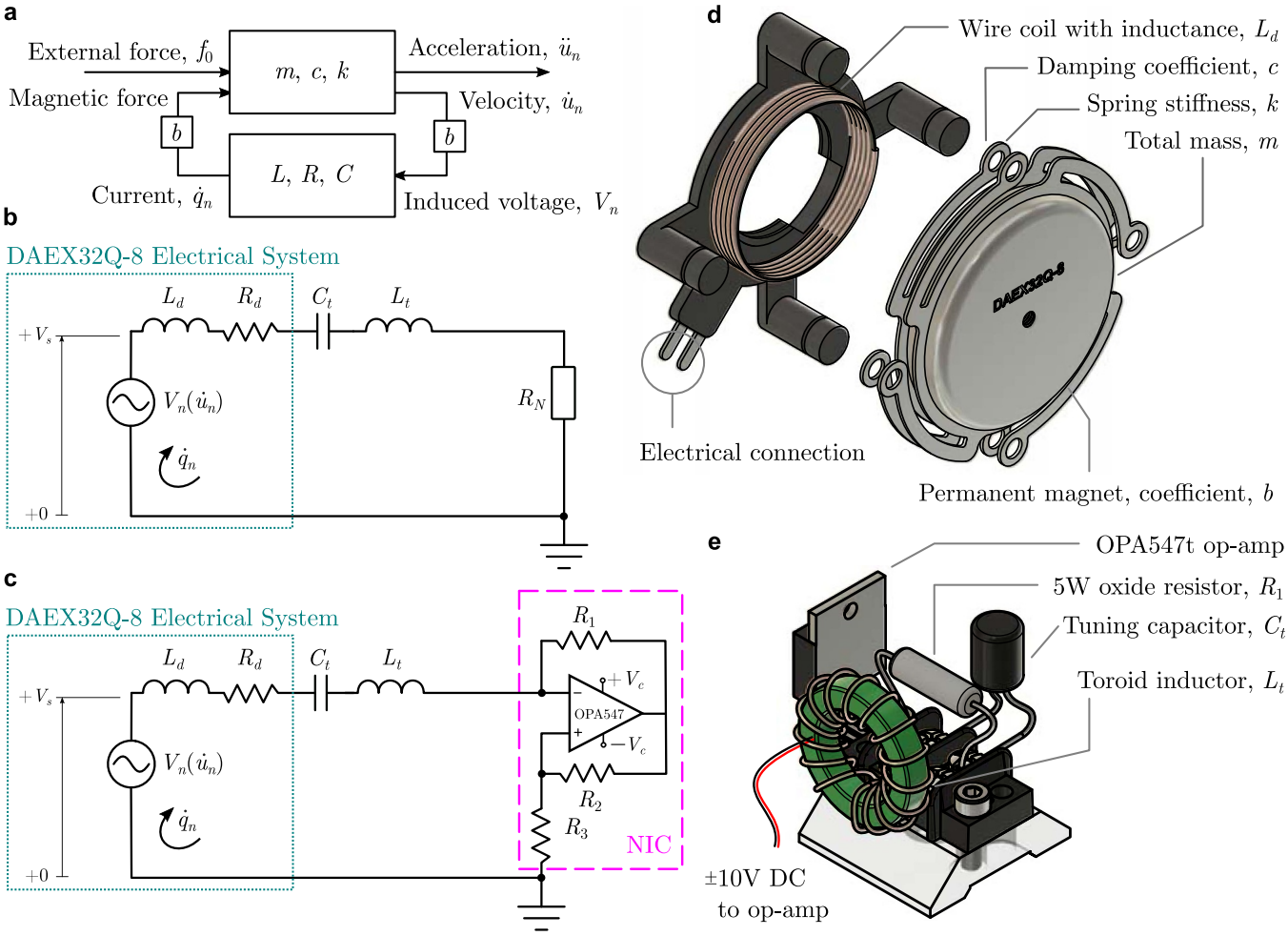

Figure 8. Experimental unit cell: (a) block diagram of unit cell operation, (b) idealized equivalent RLC circuit with internal lumped parameters and external tuning elements, (c) schematic of NIC circuit with negative resistor op-amp configuration as implemented in the experiment, (d) DAEX32Q-8 actuator which acts as unit cell, and (e) illustration of electrical unit cell.

tactile actuator from Dayton Audio: the DAEX32Q-8 (or DAEX for short). An exploded view of the DAEX is shown in figure 8(d). The DAEX is very well described by the lumped element model of one unit cell of the EMM: it consists of a large, concentrated mass (a powerful permanent magnet), four pairs of springs in parallel (total of eight curved thin beams) which have some damping, and a tightly wound electrical coil that is perfectly placed in the magnetic field of the permanent magnet but attached only to the springs such that the coil and magnet move relative to each other when one side of the actuator is fixed and the other is under some net force. The DAEX, as purchased, is equipped with a rubber mechanical damping 'boot' that connects the magnet assembly to the coil assembly, in parallel with the spring elements. The rubber boots were removed from the DAEX actuators after purchase, but this is the only modification necessary for the off-the-shelf part to function in the EMM chain. Reducing the mechanical damping inherent to the commercial DAEX actuator is simple; however, it was found that the electrical coil has a relatively large resistance which completely damps the electrical oscillations in the tuning circuit (as is common in audio actuators, speakers, etc). The electrical domain for the experimental EMM unit cell is shown in figures 8(b) and (c). The upper circuit diagram, figure 8(b), shows an ideal circuit which differentiates between the internal, inaccessible electrical elements of the DAEX—i.e. the effective inductance and resistance of the coil, as well as an idealized voltage source which represents the voltage generated from the time varying magnetic flux which is due to the motion of the magnet [45, 51]—and the tuning arm of the circuit. The intrinsic parameters are the coil inductance L_d and resistance R_d which are specified by the manufacturer as 0.36 mH and 6.5 Ohm, respectively. The tuning circuit consists of a capacitor C_t, inductor L_t, and resistor R_t. The capacitor and inductor are traditional passive lumped elements, but the resistor is considered to be variable and can take a negative value (hence the representation as a box). It was found through early experimentation, and confirmed by the theoretical frequency response functions shown in figure 5, that the total series electrical resistance in the unit cell must be less than roughly 0.50 Ohm for the EMM chain to exhibit a noticeable band gap. Therefore, the most significant barrier to overcome when employing this commercial actuator

in an EMM application is reducing the series resistance of the electrical circuit. To overcome the electrical damping, a NIC circuit was used [52].

4.2. Negative resistor tuning circuit

Negative impedance converters have been employed in many published works to realize special system properties [31–33, 53]. The NIC used in this work is unique in that it only modifies the circuit resistance: all of the desired resonant properties exist within the unit cell electrical domain already, and can be revealed with a reduction in damping. Adding a parallel resistor would be the most straightforward method of reducing the overall resistance, but a resistor cannot be placed in parallel with the inaccessible DAEX electrical system as shown in figure 8. Therefore the NIC circuit, outlined in a dashed box in figure 8(c), was employed to act as a negative resistor, thereby reducing the overall resistance. A similar tuning circuit was used by Wu *et al* with a moving coil system to attenuate acoustic waves [30]; the circuit employed here is used with the same motivation but implemented in a slightly different manner.

The gain of the operational amplifier (op-amp), OPA547T, in figure 8(c), is:

$$g_{OA} = 1 + \frac{R_2}{R_3}, \tag{38}$$

and the voltage drop across the resistor R_1 is:

$$V_I - V_A = i_1 R_1, \tag{39}$$

where $i_1 = \dot{q}_n$ is the current through the resistor, V_I is the voltage at the input terminals of the op-amp (assumed to be the same at both terminals [52]), and V_A is the amplified output voltage. Combining equations (38) and (39) we have:

$$V_I = -i_1 R_1 \frac{R_3}{R_2}. \tag{40}$$

By recognizing that the voltage at the input terminals of the op-amp, V_I, relative to ground, is the same as the voltage drop over an equivalent resistor R_N as shown in figure 8(b), we can write:

$$V_I = i_1 R_N, \tag{41}$$

with:

$$R_N = -R_1 \frac{R_3}{R_2}. \tag{42}$$

Therefore we can directly control the overall series circuit resistance,

$$R_c = R_d + R_N, \tag{43}$$

and set it to any arbitrary value through appropriate selection of the resistor values in the op-amp NIC. The total inductance is:

$$L_c = L_d + L_t, \tag{44}$$

and the capacitance of the series RLC circuit is $C_c = C_t$.

4.3. Experimental EMM unit cell

Artistic illustrations of the equipment used for one unit cell are shown in figures 8(d) and (e). The DAEX actuator (after removal of rubber boot) is shown in an exploded view and the electrical tuning circuit with op-amp and circuit elements is shown below. A single circuit part for each key element of the tuning circuit is drawn in figure 8(e) for clarity, but the physical apparatus consists of many sub-elements (i.e. several inductors in series) as shown in figure 9(a). Each unit cell tuning circuit utilizes an OPA547T from Texas Instruments. This op-amp was specifically selected for its output current capabilities (the OPA547T is specified to be capable of sourcing 750 mA with a 6 V μs^{-1} slew rate). For the experiments presented in this work the op-amps were supplied with $+10$ V and -10 V from independent switching DC power supplies. Due to the relatively large current through the RLC circuit, 5 W metal oxide resistors in the range 1–10 Ohm were used for the resistor R_1. The resistors R_2 and R_3 are common 10 kOhm elements. The inductors are standard monolayer toroid wire-wound elements rated for 10 A; several 1 mH inductors were placed in series to achieve the desired value. The capacitors used in each unit cell were electrolytic with capacitance in the range 220–1000 μF.

4.4. EMM chain apparatus

The desired band gap tunability was experimentally verified by measuring the frequency response function of the end-mass relative to the motion of the first mass (which can be thought of in terms of the end-to-end transfer function under steady-state excitation). An EMM chain with $N = 6$ unit cells was constructed and fixed to an electrodynamic shaker (LabWorks ET126-HF) as shown in figure 9(b). The magnet of the first mass ($n = 1$) is fastened to the shaker such that its motion is controlled. Each unit cell was securely fastened to the previous one using VeroClear 3D printed brackets, and the unit cells were suspended from a support structure (out of view at top of figure 9(b) with copper wire. Five electrical unit cells were assembled on a breadboard, shown in figure 9(a) (the first unit cell has no electrical component since the magnet motion is dictated by the shaker). PCB Piezotronics 352A24 accelerometers were placed on the shaker armature fixture and on the last mass in the chain, the end-mass accelerometer is visible in figure 9(c). A schematic of the experimental setup is shown in figure 9(d), with the second unit cell and the sixth (final) unit cell highlighted. The tuning circuits, accelerometers, and excitation source are labeled in both the schematic and photographs of the setup. The shaker and accelerometers are both interfaced with a Stanford Research Systems SR780 signal analyzer, pictured in figure 9(e) along with both DC power supplies and the accelerometer sensor signal conditioner. The SR780 is equipped with a built-in transfer function measurement feature which automatically sends an excitation voltage to the source (PA151 shaker amplifier, which controls shaker) and reads the voltage on two input channels; the system then computes the magnitude and phase of the ratio of

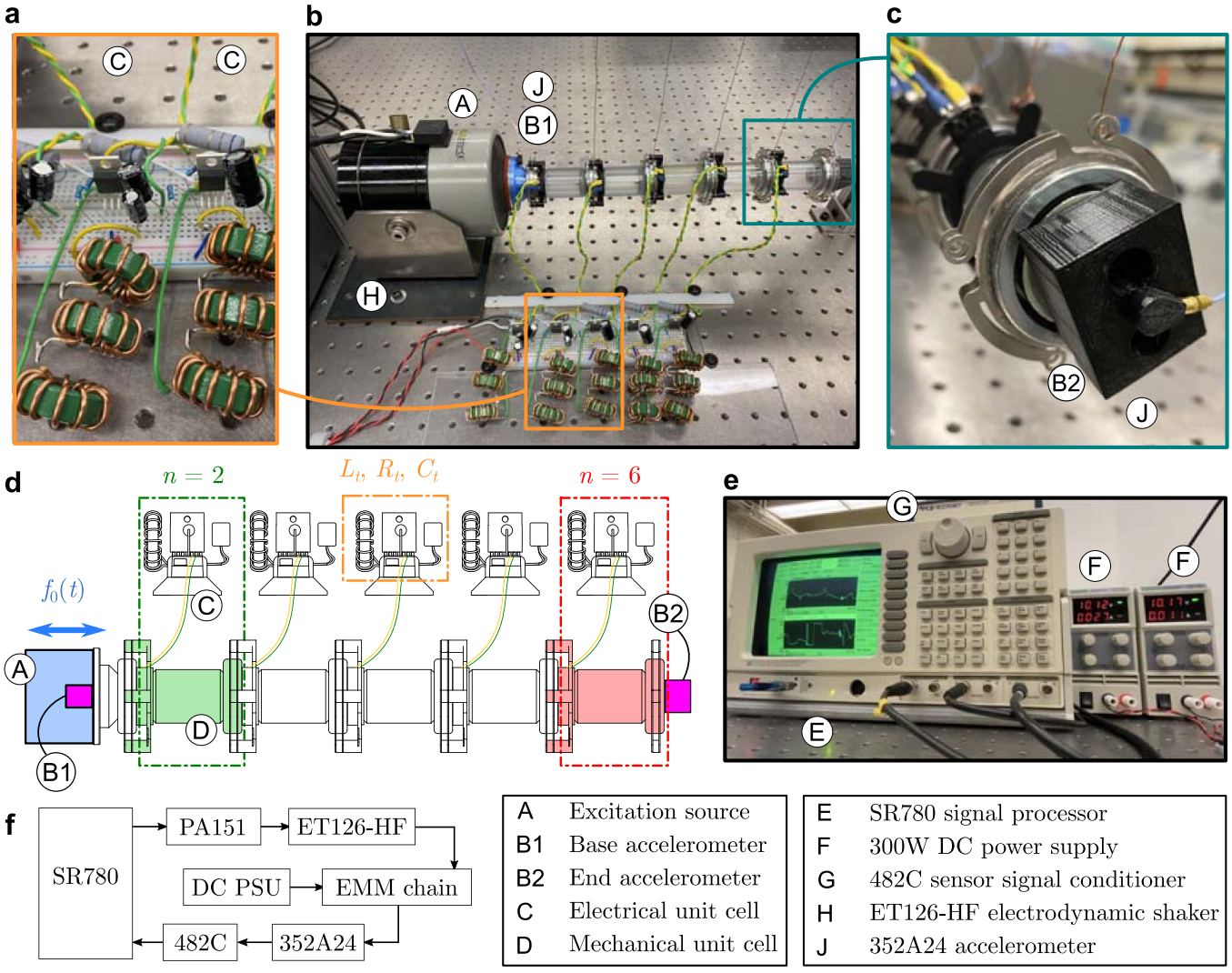

Figure 9. Experimental EMM chain apparatus: (a) close-up photo of two electrical unit cells, (b) photo of six-cell EMM chain as tested, (c) close-up photo of end mass with accelerometer, (d) schematic representation of frequency response function measurement setup, (e) signal analyzer, power supplies, and sensor signal conditioner, (f) block diagram of experimental layout.

those two channels. The experiment block diagram is shown in figure 9(f).

4.5. Theoretical data fitting methods

In order to verify the theoretical model and gain insight into the system dynamics, the experimental data was fit by solving for the optimal model parameters. The optimization was carried out using a constrained gradient based interior-point algorithm with the command `fmincon` in MATLAB. The experimental FRF magnitude and phase (assumed at steady state) was exported directly from the SR780, along with the associated frequency data. The experimental data set for one trial is defined as $\mathbf{F}_w(\mathbf{f})$ which is a 1500 element vector of FRF magnitudes (in dB) and an accompanying frequency vector $\mathbf{f}$ in Hz, and each vector has elements F_j and f_j for $j \in [1,\ 1500]$. The theoretical FRF is $H_w(2\pi f)$, where the subscript is included to distinguish between different theoretical transfer functions for different experimental cases. The theoretical FRF is a function of frequency f and depends on the theoretical parameters $\mathbf{p}_w = [m,\ c,\ k,\ L_c,\ R_c,\ C_c,\ b]$ as defined in equation (35); the FRF can be computed from the finite system state space realization. The cost function is:

$$J_w = \sum_j \left(H_w\left(f_j\right) - F_j\right)^2, \tag{45}$$

where each trial, indicated by w, gets a set of optimal system parameters $\mathbf{p}_w$. The sum is carried out over the vector index j, but the sum limits (starting and ending term) are constrained such that the cost function depends on a specific frequency range, i.e. $f_j \in [f_{\min},\ f_{\max}]$. The initial guess for the optimizer was set to the nominal value as specified by the component manufacturer, except for in the case of the damping constant c and the magnetic coupling coefficient b which were determined from separate system identification experiments on a single DAEX actuator.

The optimization step is intended to highlight the tunability of the structure. Since only one feature of the experimental

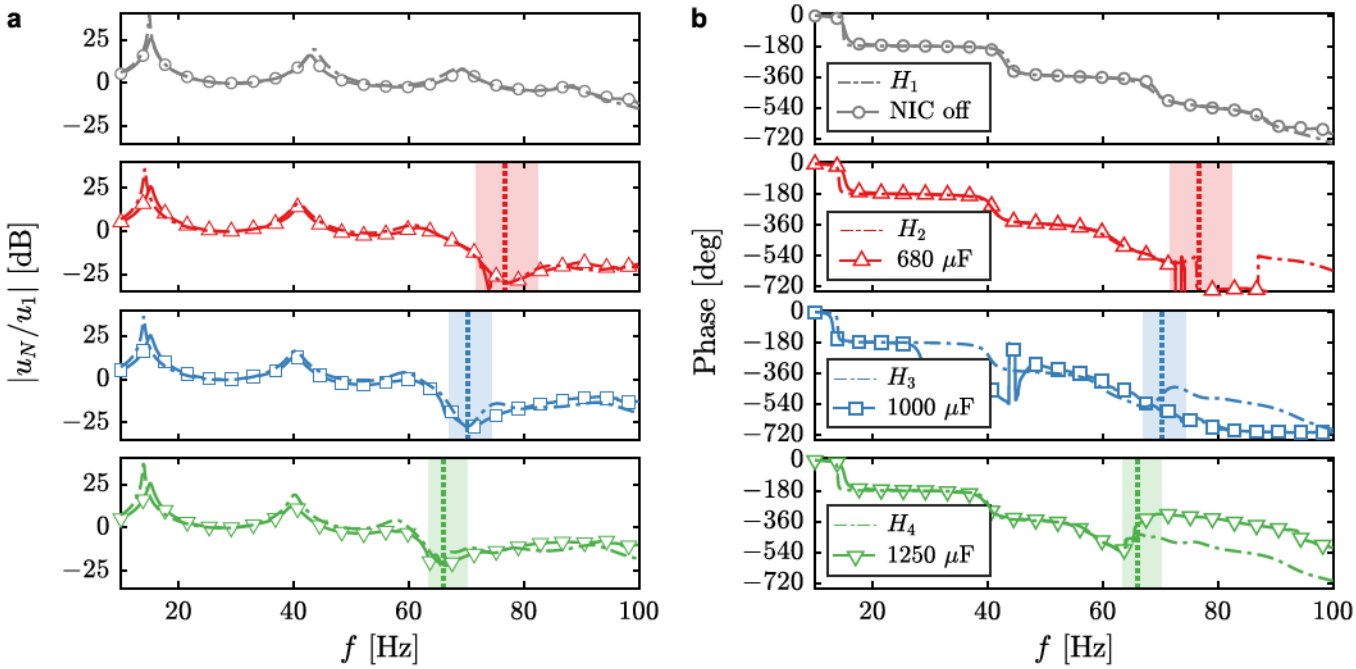

Figure 10. Experimental EMM chain results: (a) frequency response function magnitudes and (b) frequency response function phases. The top row shows the system FRF with the NIC powered off (large circuit resistance), and the remaining rows correspond to the system with the NIC powered on and varying external capacitance. Experimental data is solid line with some points highlighted with markers, theoretical prediction is dashed line. The theoretical band gap limits are indicated by a shaded area with a dotted vertical line at the maximum attenuation frequency as predicted by the dispersion relation. Note that legend entry for experimental data shows nominal capacitance value, but the theoretical fit was improved by using slightly different parameter values, see table 1.

Table 1. Theoretical frequency response function parameters used to match experimental data for varying electrical resonant frequency. For values which were experimentally measured or specified by the manufacturer, the expected value is indicated in the top row, except for the capacitance which was varied throughout the trials; the expected capacitance, C_{exp}, is shown in parentheses next to the theoretical value. Large resistance for trial 1 (H_1) means that inductance and capacitance L and C have negligible impact on frequency response curve (note that the expected resistance for this case is actually over 7 Ohm and not 0.25 Ohm since the NIC was powered off). Increasing capacitance for remaining trials (H_2, H_3, H_4) shifts band gap to lower frequency, see figure 10. The value of the cost function for the wth trial, J_w, computed with the parameters shown in the same row, is given in the last column.

H_w	m (kg)	c (kg s ^{1})	k (kN m ^{1})	L_c (mH)	R_c (Ohm)	C_c (C_{exp}) (μF)	b (Tm)	$J_w \times 10^{3}$
Exp.	0.175			3.36	0.25	Var.		
H_1	0.170	2.56	18.49	4.49	7.99	680 (N/A)	1.00	21.8
H_2	0.186	3.96	18.22	4.19	0.27	890 (680)	3.44	98.2
H_3	0.194	3.87	18.51	4.49	0.15	1015 (1000)	3.21	178.6
H_4	0.195	2.86	18.53	4.50	0.15	1141 (1220)	3.27	168.6

apparatus was changed between trials (i.e. replacing the capacitors in each unit cell for a larger valued element of the same type), it would be reasonable to fix the all the other theoretical parameters and optimize only the lumped parameter that corresponds the changed element in the setup. However, since the lumped model is an approximation, allowing all the theoretical parameters to be varied by the optimization algorithm has two benefits: first, it provides a way to account for uncertainties in the actual value of an experimental element. The electrical parameters are especially sensitive to manufacturing tolerances and may vary slightly between the actual parts. Other model parameters, such as the damping coefficient and magnetic coupling coefficient, can only be determined through system identification. Second, varying all the parameters in the model during the optimization step provides a way to account for coupling between experimental elements that is not present in the theoretical model. The electrolytic capacitors, for example, have some non-negligible resistance which varies depending on the element itself and their combination in series or parallel.

The focus of fitting the theoretical data to the experimental curves is to show quantitatively that varying the electrical tuning circuit alters the system FRF according to the trends predicted by the model. The purpose of fitting the theoretical FRF is not to precisely identify the actual model parameters; conducting a thorough system identification and a highly accurate model parameter estimation would require additional testing and more robust methodology that is beyond the scope of this work. The model optimization is included here to demonstrate that the simplified lumped-element model

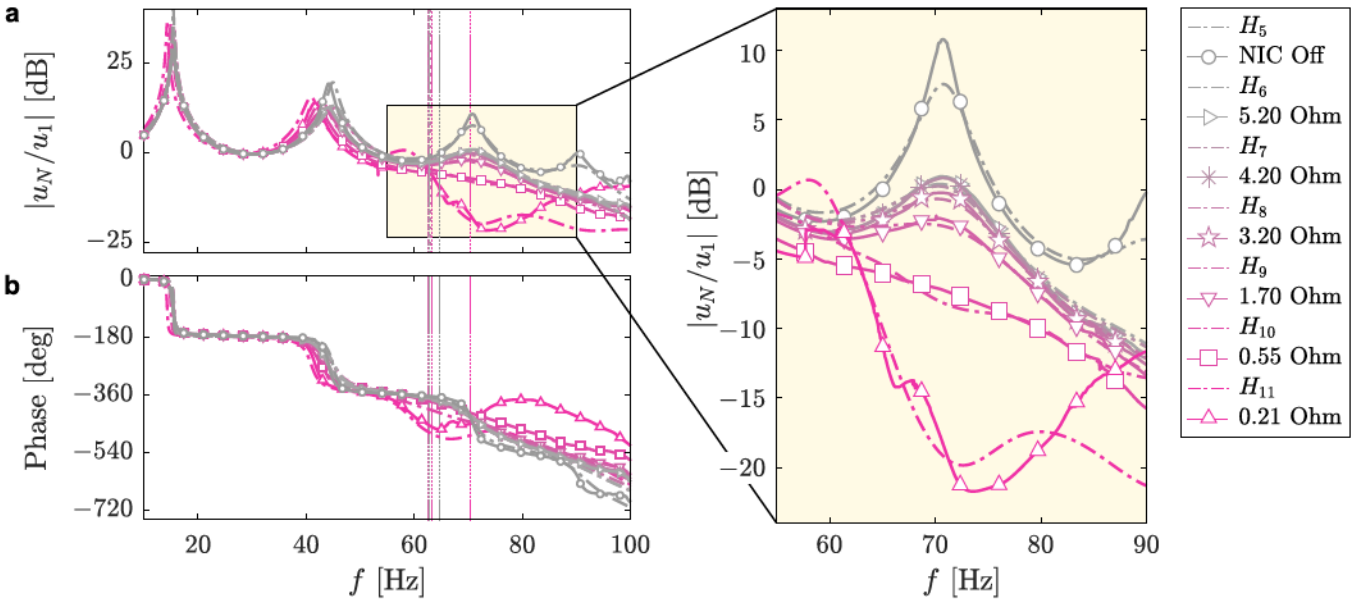

Figure 11. Experimental EMM chain results: (a) frequency response function magnitudes and (b) frequency response function phases. The band gap depth, or degree of attenuation, can be controlled by changing the total series resistance in the circuit of each local resonator. The theoretical frequency of maximum attenuation is shown as a dotted line for each case in the magnitude and phase chart, but not shown in the close-up view.

Table 2. Theoretical frequency response function parameters used to match experimental data for varying electrical damping. For values which were experimentally measured or specified by the manufacturer, the expected value is shown in the first row, with the exception of the electrical resistance which varied between trials; the expected resistance R_{exp} based on the manufacturer specifications is shown in parentheses next to the theoretical value. Large resistance for trial 1 (H_5) means that inductance and capacitance L and C have negligible impact on frequency response curve. Decreasing resistance for remaining trials increases band gap depth, see figure 11. The value of the cost function for the wth trial, J_w, computed with the parameters shown in the same row, is given in the last column.

H_w	m (kg)	c (kg s^{-1})	k (kN m^{-1})	L_c (mH)	R_c (R_{exp}) (Ohm)	C_c (μF)	b (Tm)	$J_w \times 10^{-3}$
Exp.	0.175			3.36	Var.	1000		
H_5	0.159	2.00	18.50	4.99	7.79 (7.00)	1100	3.09	8.68
H_6	0.158	3.96	18.49	4.97	4.64 (5.20)	1101	3.98	7.67
H_7	0.158	3.74	18.50	4.99	3.99 (4.20)	1100	3.99	9.16
H_8	0.157	4.00	18.49	4.99	3.46 (3.20)	1099	3.99	24.51
H_9	0.156	3.83	18.50	4.99	2.08 (1.70)	1105	3.99	14.27
H_{10}	0.169	3.76	18.50	4.99	0.62 (0.55)	1109	3.61	7.85
H_{11}	0.186	3.99	18.49	4.00	0.35 (0.21)	1049	4.00	68.7

as derived provides a qualitatively good description of the system dynamics, and quantitatively follows the trends predicted in the previous sections. Further, as the optimization algorithm itself is relatively simple, it is expected that variations between trials will occur due to the intricate numerical dependencies and the basic cost function formulation.

4.6. Variable electrical local resonance frequency

A set of experimental transfer functions are shown in figure 10 for four experimental trials, along with the theoretical predictions for the same cases. The experimental curves are shown as solid lines with intermittent markers for clarity, and the theoretical transfer functions are superimposed on the experimental charts as a dot-dashed lines. The plot legend indicates the nominal capacitance value in the tuning RLC circuit for the experimental data, and the transfer function name for the theoretical curves. The theoretical transfer functions are all $H_{N,1}$ as given in equation (35), but each has a different set of system parameter values, hence the new name subscript H_w where w indicates the specific trial of interest (1, 2, 3, or 4). The theoretical transfer functions were fit to the experimental data within the frequency range $f \in [30, 100]$ Hz. The theoretical predictions for the EMM behavior use the parameters listed in table 1, and the theoretical curves agree very well with the experimental data. The first row of model parameters, H_1, corresponds to the experimental trial conducted with the NIC powered off; for this case the resistance is expected to be substantially higher than any other trial, and the electrical parameters have almost no impact on the FRF.

The capacitance column in table 1 is the most important for placing the locally resonant band gap in these experiments: since the inductance of the tuning circuit was not varied, the band gap frequency range can be shifted by increasing or

decreasing the tuning capacitor. The nominal values shown in the legend of figure 10 differ slightly from the theoretical values which provide the best fit shown in table 1, but the trend predicted in the previous sections is confirmed: when the capacitance of the tuning circuit is increased, the FRF band gap can be observed to shift to lower frequencies. Additionally, the band gap bounds and frequency of maximum attenuation, computed from the dispersion relation, are in good agreement with the visible band gap region in the FRFs and the frequency of minimum FRF magnitude.

4.7. Variable electrical local resonator damping

A similar set of experimental trials was conducted with varying electrical resistance, the results of which are shown in figure 11. The total series resistance was reduced by increasing the value of the feedback resistor R_1 in the NIC circuit; the resistors were 7, 5.1, 3.3, 1.0, and parallel 1.2 and 1.0 Ohm elements. Figure 11(a) shows the frequency response function, and the zoomed view demonstrates the dramatic variation in frequency attenuation within the band gap region. The FRF phase is shown in figure 11(b). The theoretical transfer functions were fit to the experimental data within the frequency range $f \in [60, 85]$ Hz. The vertical dotted lines indicate the frequency of maximum attenuation as predicted by the dispersion relation for the optimal theoretical parameters in each case. The theoretical system parameters which yield the dot-dashed curves are given in table 2. The tunability of the band gap depth is shown quantitatively in table 2: as the total series resistance in the electrical system is decreased from 7 to 0.21 Ohm (corresponding to model parameter values of 7.79 and 0.35 Ohm), the band gap opens where there was previously a resonant peak. The variation in the other model parameters is notable, but they are generally near the expected value.

It is important to note that the model parameter optimization is not intended to provide a comprehensive or quantitatively precise description of the experimental system. Such a detailed and thorough system identification procedure would require a more in depth analysis of the experimental results. The values given in tables 1 and 2 are intended to demonstrate that the key traits of the system, the dependence of the band gap on tuning circuit resonance frequency and resistance, have been experimentally verified and the model is in good agreement with the experimental FRF.

5. Conclusion

This work presented the theoretical description and experimental validation for a new class of EMM chain. The metamaterial chain is distinct from those presented in previously published works in that it relies on magnetic field interactions between a permanent magnet fixed to the mechanical unit cell and the field generated within an electrical coil that is coupled to an external resonant electrical circuit. The EMM chain exhibits a tunable band gap that can be placed at a desired frequency via appropriate selection of circuit inductance and capacitance. Additionally, the magnetic field strength was shown to directly control the band gap width, and the electrical resistance was shown to directly control the band gap depth. The local resonance frequency was proven, theoretically and experimentally, to control the upper limit of the band gap–not the frequency of maximum attenuation, as would be the case in a mechanical local resonance system. The theoretical description of the metamaterial chain also revealed that the system dynamics are highly dependent on the electrical damping; a thorough investigation into this new form of electrically damped unit cell showed that the system can readily exhibit electrical metadamping. The critical interaction between damping and local resonances, which results in the electrical metadamping phenomenon, was shown to amplify the dissipation level without the need to introduce additional lossy, soft, or weak materials. Finally, the experimental apparatus was constructed from commonly available materials available from audio parts retailers at a significantly lower cost than what is commonly required for metamaterial structures, and exhibited a desirable low-frequency vibration band gap. The results of this effort indicate a significant advancement in the overall tunability and potential for simplicity and affordability in construction within the domain of EMMs, and the potential for numerous future research efforts focused on metadamping in electrically local resonant systems.

Data availability statement

All data that support the findings of this study are included within the article (and any supplementary files).

Acknowledgments

This work was done as part of a collaboration between the University at Buffalo (SUNY) and the Air Force Research Laboratory. The authors gratefully acknowledge funding from the US National Science Foundation via CMMI Award No. 1904254 and the INTERN program, as well as the Air Force Office of Scientific Research via Award No. 20RXCOR058. The authors also thank Daniel Nelson for useful discussions and insights during the modeling stage.

ORCID iDs

J Callanan https://orcid.org/0000-0001-6462-9981
C L Willey https://orcid.org/0000-0001-8147-9858
V W Chen https://orcid.org/0000-0002-6824-2757
M Nouh https://orcid.org/0000-0002-2135-5391
A T Juhl https://orcid.org/0000-0002-8946-7357

References

[1] Deymier P A 2013 *Acoustic Metamaterials and Phononic Crystals* **vol 173** (Verlag Berlin Heidelberg: Springer Science & Business Media)
[2] Hussein M I, Leamy M J and Ruzzene M 2014 *Appl. Mech. Rev.* **66** 40802

[3] Khelif A, Aoubiza B, Mohammadi S, Adibi A and Laude V 2006 *Phys. Rev.* E **74** 046610
[4] Mohammadi S, Eftekhar A A, Khelif A, Hunt W D and Adibi A 2008 *Appl. Phys. Lett.* **92** 221905
[5] Al Ba'ba'a H and Nouh M 2017 *J. Vib. Acoust.* **139** 021003
[6] Al Ba'ba'a H, Nouh M and Singh T 2017 *J. Acoust. Soc. Am.* **142** 1399–412
[7] Baravelli E and Ruzzene M 2013 *J. Sound Vib.* **332** 6562–79
[8] Claeys C C, Sas P and Desmet W 2014 *J. Sound Vib.* **333** 3203–13
[9] Al Ba'ba'a H B and Nouh M 2017 *Int. J. Mech. Sci.* **122** 341–54
[10] Al Ba'ba'a H, Nouh M and Singh T 2017 *J. Sound Vib.* **410** 429–46
[11] Ragonese A and Nouh M 2021 *Wave Motion* **105** 102734
[12] Liu Z, Zhang X, Mao Y, Zhu Y, Yang Z, Chan C T and Sheng P 2000 *Science* **289** 1734–6
[13] Colombi A, Roux P, Guenneau S and Rupin M 2015 *J. Acoust. Soc. Am.* **137** 1783–9
[14] Zhang K, Zhao P, Hong F, Yu Y and Deng Z 2019 *Smart Mater. Struct.* **29** 015017
[15] Gonella S, To A C and Liu W K 2009 *J. Mech. Phys. Solids* **57** 621–33
[16] Li J, Zhou X, Huang G and Hu G 2016 *Smart Mater. Struct.* **25** 045013
[17] Zhang X, Zhang H, Chen Z and Wang G 2018 *Smart Mater. Struct.* **27** 105018
[18] Dwivedi A, Banerjee A, Adhikari S and Bhattacharya B 2021 *Int. J. Mech. Mater. Des.* **17** 419–39
[19] Meng H, Wen J, Zhao H and Wen X 2012 *J. Sound Vib.* **331** 4406–16
[20] Attarzadeh M, Callanan J and Nouh M 2020 *Phys. Rev. Appl.* **13** 021001
[21] Chen Y, Li X, Nassar H, Norris A N, Daraio C and Huang G 2019 *Phys. Rev. Appl.* **11** 064052
[22] Nouh M A, Aldraihem O J and Baz A 2016 *J. Intell. Mater. Syst. Struct.* **27** 1829–45
[23] Lin Z, Al Ba'ba'a H and Tol S 2021 *Smart Mater. Struct.* **30** 075037
[24] Ansari M, Attarzadeh M, Nouh M and Karami M A 2017 *Smart Mater. Struct.* **27** 015030
[25] Willey C, Chen V, Scalzi K, Buskohl P and Juhl A 2020 *Appl. Phys. Lett.* **117** 104102
[26] Billon K, Ouisse M, Sadoulet-Reboul E, Collet M, Butaud P, Chevallier G and Khelif A 2019 *Smart Mater. Struct.* **28** 035007
[27] Candido de Sousa V, Sugino C, De Marqui Junior C and Erturk A 2018 *J. Appl. Phys.* **124** 064505
[28] Casadei F, Delpero T, Bergamini A, Ermanni P and Ruzzene M 2012 *J. Appl. Phys.* **112** 064902
[29] Willey C, Buskohl P and Juhl A 2020 *J. Mech. Phys. Solids* **137** 103873
[30] Wu B, Zhou W, Bao R and Chen W 2018 *J. Appl. Mech.* **85** 031004
[31] Zhu R, Chen Y, Barnhart M, Hu G, Sun C and Huang G 2016 *Appl. Phys. Lett.* **108** 011905
[32] Chen Y, Huang G and Sun C 2014 *J. Vib. Acoust.* **136** 061008
[33] Chen Y, Hu G and Huang G 2017 *J. Mech. Phys. Solids* **105** 179–98
[34] Li X, Chen Y, Hu G and Huang G 2018 *Smart Mater. Struct.* **27** 045015
[35] Bao B, Lallart M and Guyomar D 2020 *Int. J. Mech. Sci.* **172** 105423
[36] Sugino C, Ruzzene M and Erturk A 2018 *J. Mech. Phys. Solids* **116** 323–33
[37] Frazier M J and Hussein M I 2016 *C. R. Physique* **17** 565–77
[38] Hussein M I and Frazier M J 2013 *J. Sound Vib.* **332** 4767–74
[39] Aladwani A and Nouh M 2020 *Int. J. Mech. Sci.* **173** 105459
[40] DePauw D, Al Ba'ba'a H and Nouh M 2018 *Extreme Mech. Lett.* **18** 36–44
[41] Bacquet C L, Al Ba'ba'a H, Frazier M J, Nouh M and Hussein M I 2018 *Adv. Appl. Mech.* **51** 115–64
[42] Aladwani A and Nouh M 2021 *J. Appl. Mech.* **88** 1088517
[43] Frazier M J and Hussein M I 2015 *J. Acoust. Soc. Am.* **138** 3169–80
[44] Preumont A 2006 *Mechatronics* (Berlin: Springer)
[45] Falaize A and Hélie T 2020 *Acta Acust.* **4** 1
[46] Gross C A 2006 *Electric Machines* (Boca Raton, FL: CRC Press)
[47] Fitzgerald A E, Kingsley C, Umans S D and James B 2003 *Electric Machinery* vol 5 (New York: McGraw-Hill)
[48] Mead D J 1975 *J. Sound Vib.* **40** 1–18
[49] Pastor M, Binda M and Harčarik T 2012 *Proc. Eng.* **48** 543–8
[50] Rixen D J 2004 *J. Comput. Appl. Math.* **168** 383–91
[51] Kinsler L E, Frey A R, Coppens A B and Sanders J V 1999 *Fundamentals of Acoustics* (New York: Wiley)
[52] Chen W K 2002 *The Circuits and Filters Handbook* (Boca Raton, FL: CRC Press)
[53] Wu K, Huang L, Zhang X, Liu X, Wang C and Zhang Y 2021 *Int. J. Mech. Sci.* **200** 106447